TWO YEARS OF INTEGRAL MONITORING OF GRS 1915+105
PART 2: X-RAY SPECTRO-TEMPORAL ANALYSIS

J. Rodriguez[1], S.E. Shaw[2], D.C. Hannikainen[3], T. Belloni[4], S. Corbel[1], M. Cadolle Bel[5], J. Chenevez[6], L. Prat[1], P. Kretschmar[5], H.J. Lehto[7], I.F. Mirabel[8], A. Paizis[9], G. Pooley[10], M. Tagger[11], P. Varnière[12], C. Cabanac[2], O. Vilhu[3]

Draft version December 3, 2007

ABSTRACT

This is the second of two papers presenting the results of two years of monitoring of GRS 1915+105. We focus here on the results obtained at X-ray energies with *INTEGRAL* and *RXTE* and in the radio with the Ryle Telescope at 15 GHz. We present the X-ray spectral and temporal analysis of four observations which showed strong radio to X-ray correlations. During one observation GRS 1915+105 was in a steady state, while during the three others it showed cycles of X-ray dips and spikes (followed by radio flares). We present the time-resolved spectroscopy of these cycles with the view to understand the X-ray to radio connection. Our spectral analysis shows that in all cases the hard X-ray component, which we interpret as the Comptonized emission from a coronal medium, is suppressed in coincidence with a soft X-ray spike that ends the cycle. We interpret these results as evidence that the soft X-ray spike is the trigger of the ejection, and that the ejected medium is the coronal material. In addition, we study the rapid variations, and report the presence of a low frequency QPO with variable frequency during all X-ray dips observed by *RXTE*. The ubiquity of the LFQPO during the dips, prior to the ejection, may indicate a physical link between those phenomena. In the steady state observation, the X-ray spectrum is indicative of the hard-intermediate state, with the presence of a relatively strong emission, above 40 mJy at 15 GHz. The X-ray spectra are the sum of a Comptonized component and an extra power law extending to energies >200 keV without any evidence for a cut-off. We observe a possible correlation of the radio flux with that of the power law component, which may indicate that we see direct emission from the jet at hard X-ray energies. We also present the energy dependence of a ~ 4 Hz Quasi-Periodic Oscillation of constant frequency present during the hard-intermediate state observation. This QPO-"spectrum" is well modeled by a power law with a cut-off at an energy about 11 keV. We show that the energetic dependences of the QPO amplitude and the relative contribution of the Comptonized component to the overall flux are clearly different. This may rule out models of global oscillations of the Compton corona.

Subject headings: accretion, accretion disks — black hole physics — stars: individual (GRS 1915+105, XTE J1550−564) — X-rays: stars

1. INTRODUCTION

X-ray binaries and microquasars are known to be sources of copious X-ray emission from a few hundred eV up to the MeV range in some cases. This high energy emission is commonly attributed to a thermal accretion disk for the softer X-rays (below approximately 10 keV), while no real consensus has yet been found for the so-called hard X-ray tails that can be detected up to the MeV range (e.g. Grove et al. 1998). This emission is usually attributed to an inverse Compton process of the soft (disk) photons on a distribution of electrons thought to represent a corona whose geometry is a matter of debate.

The electrons can have a Maxwellian distribution of their velocity (thermal Comptonization), or not. They can represent an hybrid population (thermal and non-thermal Comptonization, e.g. Poutanen & Svensson 1996), or be in free falling inflow with bulk motion (e.g. Laurent & Titarchuk 1999). Alternatives to pure Comptonization exist. In states showing the presence of an optically thick compact jet, the high energy emission could also originate from Synchrotron Self-Compton (SSC) radiations from the jet (e.g. Markoff, Nowak & Wilms 2005). The relative strength of the spectral components together with the behavior of microquasars in the temporal domain at

[1] Laboratoire AIM, CEA/DSM - CNRS - Université Paris Diderot, DAPNIA/SAp, F-91191 Gif-sur-Yvette, France

[2] School of Physics and Astronomy, University of Southampton, SO17 1BJ, UK

[3] Observatory, PO Box 14, FI-00014 University of Helsinki, Finland

[4] INAF-Osservatorio Astronomico di Brera, via Bianchi 46, 23807 Merate, Italy

[5] European Space Astronomy Centre (ESAC) Apartado/P.O. Box 78, Villanueva de la Cañada, E-28691 Madrid, Spain

[6] Danish National Space Center, Technical University of Denmark, Juliane Maries Vej 30, 2100 Copenhagen, Denmark

[7] Tuorla Observatory and Department of Physics, University of Turku Väisäläntie 20, FI-21500 Piikkiö, Finland

[8] European Southern Observatory, Chile. On leave from CEA-Saclay, France

[9] IASF Milano-INAF, Via Bassini 15, 20133 Milano, Italy

[10] Astrophysics, Cavendish Laboratory, J.J. Thomson Avenue, Cambridge CB3 0HE, UK

[11] Service d'Astrophysique (UMR AstroParticules et Cosmologie), CEA Saclay 91191 Gif-sur-Yvette, France

[12] LAOG, Université J. Fourier (UMR5571), Grenoble, France

frequencies typically > 0.1 Hz led to the identification of the so-called spectral states (e.g. Remillard & McClintock 2006; Homan & Belloni 2005, for recent definitions). Following the changes of spectral states in these sources using a multiwavelength approach is the only way to probe the physics of accretion and its connection with the jets.

In this respect, GRS 1915+105 is probably one of the best microquasars to perform such studies. It is one of the brightest X-ray sources in the sky and it is a source of superluminal ejections (Mirabel & Rodríguez 1994), with true velocity of the jets $\geq 0.9c$. It is also known to have a strong compact jet during its periods of "hard" and steady X-ray states (e.g. Fuchs et al. 2003), while multiwavelength approaches have shown a clear connection between the presence of soft X-ray dip/spike sequences (hereafter X-ray cycles) followed by plasma ejections (Mirabel et al. 1998; Fender & Pooley 1998). An complete review on GRS 1915+105 can be found in Fender & Belloni (2004). GRS 1915+105 has been extensively observed with the *Rossi X-ray Timing Explorer* (*RXTE*) since 1996. A rich pattern of variability has emerged from these data with time scales ranging from years down to 15 msec (e.g. Morgan, Remillard & Greiner 1997). Belloni et al. (2000), classified all the observations into 12 separate classes, which could be interpreted as transitions between three basic spectral states: a hard intermediate one (State-C), and two soft intermediate ones (State-A and State-B) following the classification of Homan & Belloni (2005). Note that State-A is much dimmer and softer than State-B that is the brightest state of all three.

This is the second of two papers reporting the results of two years of an extensive monitoring campaign involving several instruments, namely *RXTE*, the Ryle Telescope (RT), and *INTEGRAL*, the latter being the main observatory of our campaign. In Rodriguez et al. 2007 (hereafter Paper 1) we presented the results of the multiwavelength analysis. In particular, we focused on four particular observations. These four observations were choosen because of the availability of simultaneous radio and X-ray observations. In all four of them the radio to X-ray connections could then be studied in great details, and showed interesting links. In three of them we found clear associations between the X-ray behavior of the source and the occurrence of radio flares. In the fourth one, the level of radio emission was rather steady and indicative of a compact jet. In Paper 1, we generalized the fact that (non-major) discrete ejections always occur as a response to an X-ray cycle composed of an X-ray dip longer than 100 s ending in an X-ray spike. Based on a model-independent analysis, we also suggested that the spike was the trigger of the ejection. We also found a possible correlation between the duration of the X-ray dip and the amplitude of the radio ejection, which may suggest that energy and/or matter accumulated during the dip, are later ejected.

In this paper we focus on the X-ray spectral and temporal analysis of those four particular observations. We start by describing the methods of data reduction in Section 2. In Section 3, we present the results, which are discussed in the last part of the paper.

2. OBSERVATIONS AND DATA REDUCTION

The log of all observations can be found in Paper 1. In this paper we focus on Obs. 1, 2, 4, 5 and particularly on the intervals that we identified as belonging to classes ν, λ, χ, and β respectively Belloni et al. (2000). To summarize, classes ν, λ, and β show occurrences of spectrally hard X-ray dips of several hundred of second longs ended by a very bright X-ray spike, marking the return to a softer state (State-A). These are followed by periods of intense and very variable X-ray activity indicative of State-A to State-B transition. We refer to these intervals (hard dips to soft spike) as cycles. Fig. 1 shows zooms on cycles from each of the three observations. During class χ GRS 1915+105 has a relatively steady level of X-ray emission, over long times. It is in that case in the hard-intermediate state, and usually shows rapid (>1 s) variability and presence of Low Frequency QPOs.

2.1. *INTEGRAL data reduction*

The data were reduced with the `Off Line Scientific Analysis (OSA)` v7.0 software. Our first step was to produce ISGRI images in two energy bands, 20–40 and 40–80 keV, in order to detect the active sources of the FOV which have to be taken into account in the (spectral and temporal) extraction processes. This list of "bright" sources was then given as an input for the extraction of IBIS/ISGRI spectra and light curves. This is a necessary process since all bright sources in the field of view can be considered as contributing to the background for the others. This means that we extracted spectra and light curves from between 5 and 8 sources. In the case of JEM-X the spectra were extracted from unit 1 of the detector[13]. For both detectors (IBIS and JEM-X) the latest versions (provided with `OSA 7.0`) of the response matrices were used in the spectral fitting. Note that due to the high variability of GRS 1915+105 accumulating spectra over the entire observation is meaningless most of the time. In the four observations we discuss here, we extracted time-resolved spectra based on selected good times intervals (gti). The JEM-X light curves were extracted with a time resolution of 1s between $\sim$ 3–13 keV, and further rebinned to 20 s. The ISGRI light curves were extracted between 18–50 keV with a time resolution of 20 s, and further rebinned to 100 or 200 s.

We should remark here that since GRS 1915+105 is very bright in the soft X-rays good quality spectra are obtained even with short accumulation times. This is, however, not the case above 20 keV. We therefore used different binning of the redistribution matrix file (rmf) during the extraction process to obtain the spectra of the best possible quality. The resultant spectra were fitted in `XSPEC` v.11.3.2t, between 5 and 20 keV for JEM-X[14], and 18 and 300 keV for ISGRI. In most cases, the spectra were further rebinned so as to obtain good quality spectra (especially in the case of short accumulation times). We added 3 % systematics to the uncertainties in the JEM-X spectra, and 2% to the ISGRI ones before the fitting process. In all fits a normalization constant was added to account for uncertainties in

---

[13] JEM-X unit 2 has been switched off since March 08, 2004

[14] Except in the case of Obs. 4 where the JEM-X spectra were fitted between 3 and 20 keV since comparison with a simultaneous PCA spectrum showed a good agreement between both detectors.

the cross calibration of the instruments. If frozen to 1 for the ISGRI spectrum, it is usually found to be between 0.9 and 1.1 for JEM-X. Since SPI is less sensitive than ISGRI below 200 keV we do not analyze SPI data in the study presented here.

2.2. *RXTE data reduction*

The *RXTE* data were reduced with `LHEASOFT` v. 6.1.2. following standard criteria for the definition of good times intervals (elevation above Earth limb greater than 10° and offset pointing less than 0.02°). We first produced light curves in several energy ranges to produce color-color diagrams, hardness ratio, and hardness intensity diagrams (HID). For the latter purpose, we extracted 16 s light curves from the top layer of PCU 2 in four energy ranges, namely 2–126 keV (channels 0–255), band 1 = 3.28–6.12 keV (channels 8–14), band 2 = 6.12–10.22 keV (channels 15–24), and band 3 = 14.76–40.41 keV (channels 36–95). These light curves were background corrected before producing hardness ratio (or colors) defined as follows: HR1 = band 2/band 1 and HR2 = band 3/band 1. Note that the background files were produced with the latest version of the saa-history file, release after the discovery of gaps in the former file.

In the case of Obs. 4 (the steady state observation; Paper 1), we extracted PCA and HEXTE spectra from the unique interval that was simultaneous with *INTEGRAL* observation and observation from the RT. The procedure is the same as that described in Rodriguez et al. (2003), again apart from the newer version of the reduction software, and the background maps used here, that are the latest made available by the XTE SOF.

For the production of high temporal resolution light curves and Fourier analysis of the PCA data, the data were reduced in the same way as presented in Rodriguez et al. (2004) (except for the different versions of the software). We extracted ~ 4 ms resolution light curves from `Binned` data format covering the 2–15 keV energy range and ~ 1 ms light curves from `Single Bit` and `Event` data format respectively covering the ~ 5–15 keV and 15–60 keV energy ranges (we restricted the highest absolute spectral channel to 150 for the latter). We then produced power density spectra from the combined 2–60 keV (Nyquist frequency of 128 Hz) and 5–60 keV light curves (Nyquist frequency of 512 Hz) to study the presence of low and high frequency quasiperiodic oscillations (LFQPO, HFQPO). Note that for the production of dynamical PDS, or PDS from a large energy range, the background correction can be neglected for the estimate of the fractional RMS variability.

For Obs. 4 we also produced energy dependent PDSs in a manner similar to that presented in Rodriguez et al. (2004), i.e. extracting ~ 4 ms light curve from about 20 spectral channels covering the 2–40 keV range. In that case the RMS amplitudes have to be corrected for the energy dependent background level. This has been done according to Berger & van der Klis (1994), i.e. $\mathrm{RMS}_{corr} = \mathrm{RMS}_{\mathrm{leahy}} \times \frac{S+B}{S}$ where $\mathrm{RMS}_{\mathrm{leahy}}$ is the RMS obtained from the Leahy normalized PDS (non background corrected), $S + B$ is the raw count rate, and S the net count rate of the source.

3. RESULTS OF THE HIGH ENERGY OBSERVATIONS

We focus here on the observations for which we obtained simultaneous X-ray and radio observations (Paper 1). Amongst them, we distinguish Obs. 1, 2 and 5 for which we observed sequences of X-ray dip/spikes (X-ray cycles) followed by radio flares, and Obs. 4 during which GRS 1915+105 is found in the steady χ class, and shows a relatively steady level of radio emission around 40–80 mJy (Paper 1).

3.1. *Time-resolved spectroscopy and models for the spectral fittings of the cycles*

All cycles from all classes show similar repeating patterns although their time constants are different. For example class λ looks very much like class β, except that the sequences in the cycle seem to occur faster (Belloni et al. 2000). We can distinguish, in each cycle, at least three intervals (Fig. 1) with common characteristics (paper 1). Interval I is the spectrally hard X-ray dip, interval II corresponds to a precursor spike ending the dip, and interval III is a spectrally very soft dip immediately following the precursor spike. In the case of class ν we identified an additional interval (Int. IV) corresponding to the major spike following the whole sequence (Fig. 1, left), while in class λ three more intervals have been identified (Fig. 1, middle). A major soft X-ray spike of about 600 cts/s (Int. IV), followed by a dip in both soft and hard X-rays (Int. V), and a return to a high degree of soft and hard X-ray emission (Int. VI). Since ejections seem to always occur after such cycles during classes ν and β (e.g. Klein-Wolt et al. 2002), we extracted time-resolved spectra from all cycles, and further averaged those belonging to the same type of interval in those two observations. On the other hand it is the first time a radio flare is observed in class λ (Paper 1). Since we cannot, a priori, know whether radio flares occur in response to each of these cycles, we extracted time-resolved spectra from this particular cycle only. Note that the ubiquity of the accretion-ejection links during cycles seen in all other classes, indicates that each λ cycle is probably followed by an ejection.

During the spectral fittings, we tested several models, starting with the phenomenological family based on a power law tail at high energy plus a thermal component at low energy modified by interstellar absorption. Note that in all fits, the absorption column density, N_{H}, was frozen to 5.7×10^{22} cm^{-2} a value well within the 5–6$\times 10^{22}$ cm^{-2} range of value usually found in the literature (e.g. Belloni et al. 2000). Note that varying N_{H} within this range does not affect the results of the spectral analysis significantly. This is especially true when considering the spectra above 5 keV. Because of a more accurate treatment of the inner regions of the disk, we used the `ezdiskbb` model (Zimmerman et al. 2005), which assumes zero torque at the inner boundary of the disk. For Obs. 2 the statistics are not good enough to find other spectral features, or fit the data with more sophisticated models. A high energy cut-off is needed in intervals I$_\nu$ and I$_\beta$. Since a power law with an exponential cut-off is usually interpreted as due to thermal Comptonization, we then fitted all spectra of classes ν and β with a model consisting of interstellar absorption, a thermal component (`ezdiskbb` when needed) and a Comptonized component (`comptt`, Titarchuk (1994)). The tem-

perature of the seed photons for Comptonization was set equal in all cases to that of the inner disk (except when the disk is not needed, and was then frozen to 0.7 keV, the temperature below which no disk component can be detected in JEM-X above 5 keV). In some cases the optical depth of the Comptonized component tends to very low values, while the electron temperature is quite high and poorly constrained. In this ranges of parameters we are outside the range of validity for this particular model. They correspond to spectral-states A and B (in the classification by Belloni et al. 2000) equivalent to steep power law/soft intermediate states, in which the coronal medium is very tenuous, and the population of electrons is probably non-thermal. The shape of the spectrum is then equivalent to a power law with no cut-off. In those cases the τ parameter was frozen to 0.01, which is the value towards what usually tended the parameters, the smallest value allowed in XSPEC . Note that although these caveats concerning the model used for the fitting, we preferred it to the phenomenological one because it 1) avoids the mixing of the two components at low energy (ie no overstimate of the contribution of the corona below $3kT_{seed}$) that is unavoidable with a simple power law model. 2) we are interested in the relative variations of the 3–50 keV flux thus well bellow the supposed kT_e, in other words where the shape of the spectrum is power law-like. 3) The use of the same model allows a true and robust comparison of the fluxes in the different intervals. Although when τ is very low and kT_e very high the interpretation in terms of thermal Comptonization is thus dubious, in terms of fluxes the relative contributions of each model component to the total flux are, therefore, more reliable. Note that similar evolutions of the fluxes are seen when fitting with the phenomenological model. This shows our method is valid. The best-fit parameters for all intervals of the three observations are reported in Table 1, while Fig. 2 shows the particular example of the four spectra from Obs.1/Class ν with the best model and individual spectral components superposed.

In all three observations the disk temperature increased smoothly through the cycle, with a simultaneous decrease of its inner radius (Table 1). Its overall contribution to the total 3–50 keV flux also increased accordingly. On the other hand the 3–50 keV contribution of the Comptonized component was never so monotonic. In class ν it first increased from I_ν to II_ν, and was then reduced by a factor of 2.2 from II_ν to III_ν. It recovered at a higher level (a factor of approximately 1.7 higher) in IV_ν. A very similar evolution is seen in Obs. 5/Class β where the Comptonized component sees its 3–50 keV flux reduced by a factor 6.7 between II_β III_β. During Obs. 2/class λ the disk appeared during III_λ and remained at a high temperature and low radius over the remaining intervals. The flux of the hard tail (assumed to be the emission of the Comptonizing corona) first increased from I_λ to II_λ, with a small decrease in the photon index. It was not statistically required in the fit to III_λ, which likely indicates that it had disappeared. We, nevertheless, added a power law to the disk component with a photon index frozen to 2.0^{15} and estimated the upper limit on its flux. We find

that from II_λ to III_λ the power law contribution to the 3–50 keV flux was suppressed by a factor greater than 4.2 (at 3–σ), and remained at a low flux until VI_λ where it reached its highest flux over the entire cycle (Table 1).

3.2. Temporal Analysis of the cycle

The dynamical power spectra of all three observations showing X-ray cycles are shown in Fig. 3. In the case of type ν, this corresponds to a cycle that is simultaneously covered with *INTEGRAL* and *RXTE*, and followed by a radio flare. Although the dip is not entirely covered by *RXTE*, a strong feature, a low frequency QPO (LFQPO), of variable frequency can be seen. The frequency of the LFQPO seems to follow the evolution of the X-ray flux, as observed in other classes (e.g. Markwardt, Swank & Taam 1999; Rodriguez et al. 2002a,b), namely β and α.

Very similar behavior is seen during λ and β-type cycles: a strong LFQPO of variable frequency appears at the moment GRS 1915+105 enters the dip (Fig. 3). The frequency rapidly decreases, in (cor)relation with the X-ray flux. The feature ceases at the end of the dip. Because of the short time scales of the events occurring at the end of the dip in class λ and the 16-s step on which the dynamical PDS is calculated, the precise moment of the cessation of the LFQPO is quite difficult to estimate. It seems to occur somewhere between the equivalent of Int. B to D (Fig. 3). In class β the QPO is cut at the maximum of the precursor spike, and so seems to be the overall noise (Fig. 3). Note that for the two latter cycles, we do not have simultaneous *RXTE* coverage to the cycles which were followed by the radio flares. We can, hence, hypothesize that GRS 1915+105 undergoes the same behavior concerning the LFQPO during all cycles, and thus also showed a LFQPO prior to the ejections during classes λ and β. Given that this is commonly observed in GRS 1915+105, and that it has already been seen in class β (e.g. Markwardt, Swank & Taam 1999; Rodriguez et al. 2002a) in simultaneity with radio flares (Mirabel et al. 1998), this hypothesis seems quite reasonable.

3.3. Observations 4: Class χ

3.3.1. X-ray spectral analysis

During the *INTEGRAL* coverage of Obs. 4, we obtained two observing intervals with the RT and five with *RXTE* (Paper 1). The second coverage with the RT overlapped only very briefly with *INTEGRAL* and we will not discuss it further here. During the first, however, the multiwavelength coverage (Fig.4) shows that the radio flux, while being rather steady during the first 13 ks at a mean value of 44.9 mJy, increased slightly between MJD 53473.25 and 53473.30. It reached a mean level of 70.4 mJy after 53473.30 up to the end of the radio coverage on MJD 53474.42. We separated this observation into 3 intervals (I_χ, II_χ, III_χ) based on the radio behavior of the source from which we extracted *INTEGRAL* spectra. In the case of I_χ an *RXTE* pointing is also available and was added to the spectral fit.

As in the previous observations, we started with different combinations of phenomenological models. It has to

---

[15]This value is a quite standard value for BH in general. Note that freezing the photon index to values greater than 2 results in even lower limits on the flux of the hard tail component.

be noted that none of the spectra is well represented by the standard model composed of an accretion disk and a power law tail. A single absorbed power law is a very poor representation of the spectra. Fig. 5 shows the residuals in terms of number of σ between the model and the spectra. Adding a multicolor disk black body in either of its forms (diskbb, ezdiskbb) still leads to a poor representation of the spectrum (even with a Gaussian, see below). In I_χ, for example, the reduced χ^2 is 10.4 for 124 d.o.f.. Since the simple power law overestimates the spectrum at high energies, we replaced it by a cut-off power law. This provides a much better representation of the spectrum, although still not satisfactory. Again adding a disk emission does not provide a good description of the spectrum. In I_χ, for example, even after having included a Gaussian around 6.5 keV, the reduced χ^2 is 12.6 for 123 d.o.f.. The emission above > 40 keV is still underestimated. Instead of a disk emission, an extra power law improves the fit significantly (F-TEST probability of $\sim 7 \times 10^{-19}$ chance improvement). Some residuals are still visible in the iron K_α region at 6.5 keV. We therefore added a Gaussian to account for this feature. The reduced χ^2 is 1.73 (123 d.o.f.) in I_χ with this model.. The cut-off power law was then replaced by the comptt model (Titarchuk 1994). This model provided very good fits to the data and gives a better χ^2 (Table 2). All spectral parameters are reported in Table 2.

A clear evolution in terms of spectral parameters is seen between the three intervals of Obs. 4 (Table 2), especially for the power law component. The temperature of the seed photons for Comptonization is rather stable around 0.3 keV, and the Kompaanets parameter ($y = kT_e/m_ec^2 \times \max(\tau, \tau^2)$), that roughly characterizes the efficiency of Comptonization, is multiplied by a factor of about 1.1 between I_χ and III_χ. In the mean time the power law photon index of the hard tail gets softer. In terms of fluxes (unabsorbed 2–200 keV), that of the Comptonized component is divided by a factor of about 1.2 between I_χ and III_χ, while that of the hard tail is multiplied by a factor of about 1.6. The power law fluxes are significant at more than 10-σ in each intervals. Based on the errors of the power law parameters we can estimate a ratio 1.61±0.13 (1-σ error) increase of the power law flux between I_χ and III_χ.

3.3.2. *Timing Analysis: LFQPOs*

We first analyzed the 2–60 keV PDS of the unique ~ 3000 s *RXTE* pointing that was simultaneous with both *INTEGRAL* and the RT. The PDS was computed between 0.03125 Hz and 124 Hz. The PDS is composed of a flat top component up to a break frequency above which a power law decrease can be seen. On top of this continuum a strong Low Frequency Quasi Periodic Oscillation (LFQPO) is detected. Above about 20 Hz the PDS is compatible with Poissonian noise. We modeled it with the sum of a broad zero-centered Lorentzian, a narrow one (the LFQPO), and a constant to account for the white noise. The fractional RMS amplitude of the continuum of the PDS above 0.03125 Hz is $13.1 \pm 0.4\%$. The QPO centroid frequency is 3.77 ± 0.01 Hz, its quality factor Q($= \nu_{\rm centroid}/$FWHM) is 7.7, and its fractional RMS amplitude $10.9^{+0.6}_{-0.7}\%$.

This best model was used to fit the energy dependent PDSs. Note that given their poorer statistics and the fact that we are interested in the parameters of the LFQPO, we subtracted the white noise and restricted the frequency range to 0.03125–10 Hz. The energy dependence of the LFQPO (hereafter QPO spectrum) is plotted in Fig. 6. The QPO spectrum is hard in the sense that it increases with energy. A plateau and possible following decrease can be seen from 10–15 keV. Such behavior has already been reported for LFQPOs from class χ observations (Rodriguez et al. 2004). We first fitted the QPO spectrum with a simple power law model. The statistics of the fit is poor with χ^2_ν=2.05 for 14 d.o.f.. In order to account for the deviation from a simple power law (Fig. 6), we added an exponential cut-off to the power law (see Rodriguez et al. (2004)). We obtained a good representation of the spectrum with χ^2_ν=0.41 for 12 d.o.f.. The best parameters are a power law index of 0.53 ± 0.04, a cut-off energy $E_{\rm cut} = 11.3 \pm 1.3$ keV, and a folding energy for the cut-off $E_{\rm fold} = 23 \pm 6$ keV.

4. DISCUSSION

4.1. *Model-independent evolution, hardness intensity diagrams*

Fig. 7 shows two HIDs of all the *RXTE* pointings of the four observations presented in this paper (see Table 2 of Paper 1 for the journal of the entire observations). The first one, representing the PCU2 intensity vs. HR1 ((6.12–10.22) keV/(3.28–6.12) keV) (hereafter HID1) matches exactly the colors commonly used in the literature for the production of HIDs (e.g. Belloni 2005; Fender et al. 2004). However (as clearly mentioned in Fender et al. (2004)) since the thermal disk component in GRS 1915+105 is always brighter than in any other BH, using the same colors results in having the hard C-state lying in a softer part of the HID than the soft B-state (Fig. 7, left). The second HID (HID2) makes use of colors (HR2=(14.76–40.41) keV/(3.28–6.12) keV) well separated so that the disk component can clearly be separated from any other component. Although the values of the HR are quite different between the three classes with cycles, the general pattern shows striking similarities in both plots. They all have in common a "parallel" trend from the low values of intensity and HR1$\sim$ 0.5, (resp. HR2$\sim$ 0.03) to intermediate values of the intensity, and HR1$\sim$ 0.5, (resp. HR2$\sim$ 0.01). This corresponds to the dips of the cycle (at the right bottom of the tracks), and the spikes that end them. This parallel track also corresponds to the temporal evolution of GRS 1915+105 when going through the cycle. It first evolves in intensity at a high value of HR2 (or roughly constant value of HR1), and, after the spike, falls to the left part of the plots (low values of HR2 and decrease in intensity). Note that, as we show in the next section, the spike is very likely the trigger of the ejection, hence the HR2 of the spike could represent the jet line of Fender et al. (2004). Its precise value is, however, quite difficult to estimate in the three classes, as just before the ejection, the values of HR2 are clustered in a region they can reach even in the flaring state. This is quite well illustrated in Fig. 7 in the case of class λ around HR2=0.02. However we remark that each time GRS 1915+105 exits the dip of a cycle, an ejection occurs (Paper 1). The approximate

position of the jet line is represented in the right panel of Fig. 7. The flaring states of the observations correspond to oscillations between the points that lie on the left of this jet line.

4.2. *Ejection of coronal material?*

In Paper 1 we have shown that the same sequence of events will lead to the ejection of material. Namely, an X-ray dip of duration longer than 100 s terminated by an X-ray spike always precede a radio flare. We have argued, in a model-independent way, that the X-ray spike terminating the sequence was the trigger of the ejection. This was based on the similarity of the sequence of events, and that in class β the spike had been identified by Mirabel et al. (1998) as the trigger of the ejection. Here we followed a different approach, and performed fits to each remarkable interval of the cycles.

Although the precise spectral parameters returned from the fits (Table 1) show differences between the cycle of each class, a similar evolution can be seen in all. As presented in Sec. 3, while the evolution of the disk along the cycles is monotonic, and may indicate a disk that slowly reaches its last stable orbit around the BH, the evolution of the Comptonized component or the power law component (the corona) is quite different. While it entirely dominates the spectra during the hard-dips (Ints. I), it disappears after the spike labeled II in all cases, and seems absent in the soft dips (Ints. III). Its relative contribution to the source flux, in the same band as that of the disk, decreases by a minimum factor of 2.2 (in class ν).

In the case of class β Mirabel et al. (1998) demonstrated that the X-ray spike was the trigger of the ejection. In Paper 1, based on the similarities of the sequences seen during the three classes, shape, evolution of the source fluxes in different X-ray bands, and delays between the X-rays and the radio peak, we argued that the spike (II_ν, II_λ and II_β) is the very likely trigger of the ejection. Our spectral analysis is compatible with such an interpretation, since in all cases the spectra greatly evolve after the spike, and show a transition to a state dominated by the disk component. In that case, the quantitative evolution of the coronal flux shows that this component disappears between Ints. II and III. Given the detection of ejected material at approximately the same time delay in all three classes, it is tempting to consider that the corona is ejected at the spike, decoupled from the central system, and is further detected at radio wavelengths.

One could argue that the spike is not the real trigger. The other remarkable moment of each cycle (at least from the spectral point of view) is the entrance into the dip. Here the spectrum becomes hard, which likely indicates that the inner regions of the disk either recede from the BH or disappear. Several arguments do not favor this moment as being the trigger of the ejection. First the radio flares –the signature of the ejections– have similar profiles (Paper 1), while the transitions to the dip at X-ray energies are quite different, especially in their temporal evolutions. The decrease of the X-ray count rate is quite slow in ν and β, while it is quite sudden in λ. If this moment were the signature of the ejection at X-ray energies, it is reasonable to think that its temporal evolution would influence the subsequent ejection. Secondly, during class β, a 0.8 keV disk is clearly detected during the dip, while the amplitude of the ejection is higher than in class λ (no disk in the dip), and the duration of the dip is longer. This is in contradiction with a model where the longer duration dip associated with a higher amplitude ejection would indicate that more disk material is ejected, and hence it would take longer for it to be refilled. Finally the delay between the peak in radio and the spike terminating the cycle is similar in all classes (Paper 1), while the duration of the dip, and hence the delay between the transition into the dip and the radio peak is quite different between the three classes. It is around 0.8 hour in class ν, while it stays around 0.4 hour in the other two classes.

We therefore favor an interpretation where the coronal material is ejected from the system at the spike terminating the hard dips of the cycle. It is interesting to note that in another class with a cycle (class α), Rodriguez et al. (2002b) had come to the same conclusion, although based on the inspection of the evolution of HRs and light curves only (see also Vadawale et al. (2003)). Further strengthening this interpretation is the case of another microquasar, XTE J1550−546, where Rodriguez et al. (2003) arrived at the same conclusion studing the evolution of this source's outburst in 2000. The similar conclusions reached in two different sources may indeed indicate that the discrete ejections in (all) microquasars are composed of coronal material.

4.3. *Steady hard (intermediate) state*

During one of our observations, GRS 1915+105 was found in the so-called χ class of variability in the X-rays, which corresponds to its hardest steady state[16]. In the radio domain a relatively bright and steady emission is detected, and attributed to the presence of a compact jet (e.g. Fuchs et al. 2003). As mentioned in Vadawale et al. (2003) the spectrum of this radio loud χ observation indicates the presence of a Comptonizing component and an extra power law (Table 2). We do not need any thermal component at low energy, which indicates that the accretion disk is quite cold (at least it has no effect above 3 keV), and indeed the temperature of the seed photons for Comptonization is quite low, around 0.3 keV. It is interesting to note that when separating the observation into three noticeable intervals based on differences in the radio fluxes, we clearly see the spectral evolutions of the two X-ray spectral components (Table 2). While the 15 GHz flux increases, the 2–200 keV flux of the Compton component decreases, while that of the extra power law component seems to increase as well in coordination with a softening of the tail.

The spectral characteristics of radio-loud χ classes in GRS 1915+105 have been shown to always imply Comptonization by a corona of a few keV and optical depth of the order of several units (Trudolyubov 2001; Vadawale et al. 2003). This either results in spectra of shape similar to the ones we observed here (Vadawale et al. 2003), or phenomenologically with breaks at 12–20 keV (Trudolyubov 2001). Several competing models may explain the simul-

---

[16]Note that as GRS 1915+105 is never observed to be in the canonical hard state seen in other microquasars, "hard" is taken here as relative to its other spectral states. The so-called χ class/state corresponds to the hard-intermediate state in the other sources, following the definition of Homan & Belloni (2005)

taneous presence of thermal Comptonization and of an additional power law. This may be the signature of Comptonization on a hybrid thermal/non-thermal population of electrons (e.g. Poutanen & Svensson 1996). This family of model has been successfully applied to the modeling of microquasars in steep power-law/soft intermediate/very-high states showing power laws with no cut-off up to the MeV domain (Cadolle Bel et al. 2006, e.g.), or even to some peculiar classes of GRS 1915+105 (Hannikainen et al. 2005). These states were, however, never associated to a strong radio emission. Trudolyubov (2001) argued that differences between the radio loud and radio quiet χ states are related to different structures of the accretion flow around the black hole, the obvious difference being the presence or absence of a compact jet. The fact that the flux of the power law component increased in simultaneity with the radio flux from the compact jet seems to indicate a link between the hard tail and the radio emission. This correlation between the evolution of both components leads to the tempting conclusion that the hard tail seen at X-ray energies is emitted by the jet itself. This possibility may be further re-inforced by the very similar evolution of both components: the 2-200 keV flux of the hard tail increased by a factor 1.61±0.13 between I_χ and III_χ when at the same time the radio flux increased by a factor 1.57±0.14. The Pearson correlation factor between the radio and power law fluxes of the three intervals is 0.93, which suggests that the radio and power law fluxes are strongly correlated. In the case emission from the compact jet the radio emission would lie in the optically thick spectral domain, while the X-ray emission would lie in the optically thin one. Therefore a direct linear relation may therefore appear as a special case. It has to be noted that the parameters of the power law we find here are very similar to the one reported by Vadawale et al. (2003). In the latter work, these authors suggested, based on a simple modeling of a compact jet, that this additional power law could be direct synchrotron emission from the jet. The similarity of their results and our may also favor the same interpretation. The origin or possible link of the Comptonized component with the jet is less clear as inverse Comptonization can occur either on the base of the jet, or under the form of SSC of the jet photons (Markoff, Nowak & Wilms 2005). The fact that the temperature for the seed photons remains constant, at a low value, rather suggest the seed photons for Comptonization probably come from the cold disk.

As expected during class χ, a strong LFQPO is detected during the unique interval that is simultaneous to the RT and *INTEGRAL*. We confirm previous findings that the QPO spectrum shows a cut-off (Rodriguez et al. 2004), and by comparing with previous observations, we can see that the cut-off energy is clearly not constant and may evolve from one observation to another (Rodriguez et al. 2004). In Rodriguez et al. (2004) we had suggested that the spectrum of the QPO could be understood if one assumed that the high energy component was not modulated and came from a jet. Here the same conclusion holds when observing a cut-off while the power law may extend to much higher energies than the QPO does (Fig. 6 & 5). The presence of a LFQPO is always contemporaneous to the presence of a Comptonized component in the energy

spectra of the source. Whether this component is thermal or not (i.e. whether it shows a cut-off or not when modeled with power laws) depends on the source and the spectral state. Several models have attempted to explain the QPOs. One may distinguish between models based on instabilities in the disk (e.g., the Accretion Ejection Instability (AEI) Tagger et al. 2004), oscillations of the boundary between the accretion disk and an inner post-shock region (e.g. Chakrabarti & Titarchuk 1995), or even global oscillations of the disk itself (e.g. Nowak & Wagoner 1992). The correlations seen between some of the spectral parameters and those of the LFQPO as well as their intrinsic properties (e.g. Markwardt, Swank & Taam 1999; Rodriguez et al. 2002a,b; Vignarca et al. 2003; Rodriguez et al. 2004) indicate that they are tightly linked to the Keplerian orbit of the accretion disk, and to the corona itself. In order to study the possibility that the QPO represents some oscillation of the corona, we plotted in Fig. 8 the E–F_E PCA spectrum from I_χ with the different contributions superposed upon it. In the lower panel we compared the relative contribution of the comptt and power law components to the QPO spectrum. The QPO spectrum is clearly not power law like further indicating that its origin does not lie in the hard tail. The fact that this hard tail is likely the direct emission from the jet at high energy gives more strength to the suggestion of Rodriguez et al. (2004) that the jet emission do not contain any quasi-periodic modulation. Furthermore the QPO spectrum and the relative contribution of the Comptonized component, even scaled down, are clearly not compatible (Fig. 8). This may rule out models based on the oscillation of the corona, and would rather favor models of disk instability (as e.g. the AEI; Tagger et al. 2004), or global oscillations of the disk (Nowak & Wagoner 1992). The presence of strong QPO together with a strong corona may simply indicate that the corona either enhances the modulation, or simply that the QPO needs the corona to develop. In that case one has to note that whatever produces the QPO, its emission necessarily undergoes Compton up-scattering. Note that if the Compton component comes from SSC from the jet, then the large differences between two spectra (QPO and Compton) further indicates that the jet is not at the origin of the LFQPO.

5. SUMMARY

We have presented the X-ray spectral analysis of four *INTEGRAL* and *RXTE* observations of the microquasar GRS 1915+105. In this analysis we focused on intervals that were strictly simultaneous to radio observations taken with the Ryle Telescope. The results of the multiwavelength approach are reported in Paper 1, where we showed that bubble ejections always follow a sequence of a hard dip terminated by a sudden spike at X-ray energies (referred to as a cycle). We performed a fine spectral analysis of the entire cycles from a few keV up to about 100 keV for the first time in three different classes. We then presented a spectral and timing analysis of the unique observation during which GRS 1915+105 is found in a steady hard-intermediate state, and for which a strong and rather steady jet is detected in radio. The main results of our analysis can be summarized as follows:

- In all classes with cycles (ν, λ and β) we showed

that the ejection seen in radio is triggered at the spike terminating the cycle. By comparison with other such classes which always end with a large X-ray spike (e.g. θ and α), we suggest that this is a very generic behavior in GRS 1915+105.

- In the same observations, we showed that each spike is indicative of the disappearance of the Compton component from the X-ray spectra. We interpreted this as the evidence that the ejected material was the corona responsible for the Comptonized component. Again comparing with the behavior seen during other classes (Rodriguez et al. 2002b; Vadawale et al. 2003) or in other sources (e.g. Rodriguez et al. 2003) leads us to suggest that this phenomenon is very generic in microquasars.

- In all cycles a strong LFQPO with variable frequency shows up at the transition into the dip and is quenched at the X-ray spike ending the cycle. This phenomenon may indicate a strong link between the QPO, the X-ray behavior, and the subsequent ejection. In a model-dependent interpretation, this is compatible with the prediction of the AEI and the magnetic flood proposed to explain the behavior of GRS 1915+105 during class β (Paper 1 Tagger et al. 2004).

- The X-ray behavior of GRS 1915+105 during a radio loud χ observation shows the presence of two emitting media, one responsible for thermal Comptonization, and another emitting a hard X-ray tail modeled with a power law extending up to 200 keV without any break.

- We find a correlation between the radio flux and the 2–200 keV flux of the hard tail. The very similar evolution of both the radio flux, and the flux of the hard tail may suggest that this component is direct emission from the jet.

- The energy dependence of a LFQPO does not follow the energy dependence of the relative contribution of the Comptonized component, neither that of the hard tail. This indicates that the QPO does not have its origin in the jet, and may also rule out models based on oscillations of a Compton corona. Globally the behavior of the LFQPO is more compatible with models of disk instabilities.

All these points tend to show GRS 1915+105 behaves in a way very similar to other microquasars, and is certainly compatible with the generic model of Fender et al. (2004). The main difference is that its disk is never completely emptied and hence GRS 1915+105 never reaches true quiescence and undergoes cycles between bright hard intermediate and soft intermediate states. The similarity of all cycles, the possible correlation between the amplitude of the ejections and the duration of the dip at X-ray energies (Paper 1), the repeating scenario of ejection of the coronal medium, the correlated presence of LFQPO indicate a unique mechanism may be at the origin of all cycles. In the case of a β cycle Tagger et al. (2004) proposed a magnetic flood scenario compatible with these observed properties. Our monitoring campaign will continue with the view to cover many more of those cycles and better understand the connections and origin of the hard X-ray emitters to those of the radio jet

REFERENCES

Belloni, T., Klein-Wolt, M., Mendez, et al. 2000, A&A, 355, 271
Belloni, T. 2005, Interacting Binaries: Accretion, Evolution and Outcomes", eds. L. A. Antonelli, et al., Procs. Interacting Binaries Meeting, Cefalu, Italy, June 2004, astro-ph 0504185
Berger, M., & van der Klis, M. 1994, A&A, 292, 175
Cadolle Bel, M., Sizun, P., Goldwurm, A. et al. 2006, A&A, 446, 591
Chakrabarti, S.K., Titarchuk, L.G. 1995, ApJ, 455, 623
Fender, R. & Pooley, G. 1998, MNRAS, 300, 573
Fender, R.P. & Belloni, T. 2004, ARA&A, 42, 317
Fender, R.P, Belloni, T., & Gallo, E. 2004, MNRAS, 355, 1105
Fuchs, Y., Rodriguez, J., Mirabel, F., et al. 2003, A&A, 4 09, L35.
Goldwurm, A., David, P., Foschini, L., et al. 2003, A&A, 411, L223
Grove, J. E., Johnson, W. N., Kroeger, R. A., McNaron-Brown, K., Skibo, J. G., Phlips, B. F. 1998, ApJ, 500, 899
Hannikainen, D.C., Rodriguez, J., Vilhu, O., et al. 2005, A&A, 435, 995
Homan, J. & Belloni, T. 2005, Ap&SS, 300, 107
Klein-Wolt, M., Fender, R. P.; Pooley, G. G., et al. 2002, MNRAS, 331, 745
Laurent & Titarchuk 1999, ApJ, 511, 289
Nowak, M.A., Wagoner, R.V. 1992, ApJ, 393, 697.

Markoff, S., Nowak, M. A., & Wilms, J. 2005, ApJ, 635, 1203.
Markwardt, C.B., Swank, J.H., & Taam, R.E. 1999, ApJ, 513, 37
Migliari, S. & Belloni, T. 2003, A&A, 404, 283
Mirabel, I.F. & Rodríguez, L.F. 1994, Nature, 371, 46
Mirabel, I.F., Dhawan, V., Chaty, S., et al. 1998, A&A, 330, L9
Morgan, E.H., Remillard, R.A & Greiner, J. 1997, ApJ, 482, 993
Poutanen J., Svensson R., 1996, ApJ, 470, 249
Remillard, R.A. & McClintock, J.E. 2006, ARA&A, 44, 49
Rodriguez, J.,Varnière, P., Tagger, M., Durouchoux, P., 2002a, A&A, 387, 487
Rodriguez, J., Durouchoux, P., Tagger, M., et al., 2002b, A&A, 386, 271..
Rodriguez, J., Corbel, S. & Tomsick, J.A. 2003, ApJ, 595, 1032.
Rodriguez, J., Corbel, S., Hannikainen, D.C., et al. 2004, ApJ, 615, 416
Rodriguez, J., Hannikainen, D.C., Shaw, S.E., et al. 2007, submitted to ApJ, paper 1.
Shimura, T., & Takahara, F. 1995, 445, 780
Tagger, M., Varnière, P., Rodriguez, J. & Pellat, R. 2004, ApJ, 607, p. 410
Titarchuk, L. 1994, ApJ, 434, 313
Trudolyubov, S.P 2001, ApJ, 558, 276

Vadawale, S.V., Rao, A.R. & Chakrabarti, S.K. 2001, A&A, 372, 793

Vadawale, S.V., Rao, A.R., Naik, S. et al. 2003, ApJ, 597, 1023

Vignarca, F, Migliari, S., Belloni, T., Psaltis, D., van der Klis, M. 2003, A&A, 397, 729

Zimmerman, E. R., Narayan, R., McClintock, J. E., Miller, J. M 2005, ApJ, 618, 832

TABLE 1

BEST PARAMETERS OBTAINED FROM THE FITS TO THE JEM-X+ISGRI DATA OF THE SEVERAL INTERVALS OF OBS. 1, 2 AND 5.
THE FITS OF OBS. 1 CORRESPOND TO THE INTERVAL REPRESENTED IN FIG. 2. FOR OBS. 1 & 5 THE BEST FIT MODEL IS
phabs(ezdiskbb+comptt) (IN XSPEC NOTATION), WHILE FOR OBS. 2 IT IS phabs(ezdiskbb+powerlaw). THE ERRORS ARE GIVEN
AT THE 90% CONFIDENCE LEVEL. THE UPPER LIMITS ON THE FLUXES ARE AT THE 3–σ (99.73%) LEVEL.

Int.	kT_{seed} (keV)	R_{in}[a] ($\times \frac{R_G}{\sqrt{cos(i)}}$)	kT_e (keV)	τ	χ^2_ν (d.o.f.)	unabs. fluxes	
						3-50 keV disk	3-50 keV comptt
						($\times 10^{-8}$ erg cm^{-2} s^{-1})	
			Obs. 1, class ν				
I$_\nu$	0.7 (frozen)		33^{+6}_{-4}	0.6 ± 0.1	1.49 (88)		1.4
II$_\nu$	1.33 ± 0.09	$12.1^{+2.2}_{-1.7}$	14^{+8}_{-3}	$1.5^{+0.6}_{-0.7}$	1.42 (44)	2.42	1.9
III$_\nu$	$1.5^{+0.3}_{-0.2}$	$7.6^{+2.0}_{-0.6}$	90^{+57}_{-12}	0.01 (frozen)	1.30 (31)	2.66	0.86
IV$_\nu$	$2.10^{+0.06}_{-0.07}$	6.2 ± 0.3	110^{+17}_{-14}	0.01 (frozen)	1.52 (68)	7.9	1.5
			Obs. 5, class β				
I$_\beta$	0.8 ± 0.2	28^{+64}_{-14}	15^{+32}_{-5}	$1.5^{+0.5}_{-1.2}$	1.11 (43)	0.77	1.2
II$_\beta$	0.9 ± 0.4	21^{+100}_{-13}	181^{+65}_{-31}	0.01 frozen	1.20 (39)	0.89	1.6
III$_\beta$	1.5 ± 0.1	$6.2^{+1.2}_{-1.4}$	> 124[b]	0.01 frozen	1.13 (31)	1.4	0.24
			Obs. 2, class λ				
Int.	kT_{disk} (keV)	R_{in}[a] ($\times \frac{R_G}{\sqrt{cos(i)}}$)	Power law index Γ		χ^2_ν (d.o.f.)	unabs. fluxes	
						3-50 keV disk	3-50 keV PL
						($\times 10^{-8}$ erg cm^{-2} s^{-1})	
I$_\lambda$	$\cdots$	$\cdots$	$2.51^{+0.09}_{-0.11}$		1.14 (48)		0.95
II$_\lambda$	$\cdots$	$\cdots$	2.6 ± 0.2		0.95 (37)		1.2
III$_\lambda$	1.83 ± 0.09	7^{+1}_{-2}	2 frozen		0.88 (29)	4.4	< 0.29
IV$_\lambda$	$2.11^{+0.08}_{-0.07}$	6 ± 1	2 frozen		0.88 (31)	7.3	< 0.43
V$_\lambda$	2.05 ± 0.07	$5.1^{+0.9}_{-0.5}$	2 frozen		1.08 (33)	4.8	< 0.49
VI$_\lambda$	1.97 ± 0.06	5.9 ± 0.6	2.9 ± 0.3		1.49 (41)	5.4	1.9

[a]We take a correction factor f=1.9 (Shimura & Takahara 1995), M=14$M_\odot$, and D=10 kpc to convert the model normalization to R$_G$,
R$_{in}$ = 0.859 $\times \sqrt{K} \times \frac{R_G}{\sqrt{cos(i)}}$, with K the model normalization and i the inclination angle.

[b]The limit on this parameter is given at the 90% confidence level.

TABLE 2

BEST PARAMETERS OBTAINED FROM THE FITS TO THE JEM-X+ISGRI (AND PCA+HEXTE WHEN AVAILABLE) SPECTRA OF
OBS. 4/CLASS χ. THE BEST FIT MODEL IS phabs(comptt+ga+powerlaw) IN XSPEC NOTATION. THE ERRORS ON THE PARAMETERS
ARE GIVEN AT THE 90% CONFIDENCE LEVEL.

Interval	kT_{seed} (keV)	kT_e (keV)	τ	Γ	χ^2_ν (d.o.f.)	2–200 keV unabs. fluxes[a] ($\times 10^{-8}$ erg cm^{-2} s^{-1})	
						comptt	PL
I$_\chi$[b]	0.32 ± 0.01	6.66 ± 0.03	2.084 ± 0.008	2.62 ± 0.01	1.60 (122)	2.70	0.77
II$_\chi$	$0.33^{+0.06}_{-0.03}$	$6.66^{+0.34}_{-0.07}$	$2.22^{+0.2}_{-0.02}$	$2.74^{+0.02}_{-0.04}$	0.92 (52)	2.65	1.09
III$_\chi$	$0.26^{+0.04}_{-0.2}$	7.0 ± 0.1	$2.16^{+0.03}_{-0.02}$	$2.81^{+0.02}_{-0.07}$	1.25 (51)	2.32	1.24

[a]The fluxes are those from *INTEGRAL*/ISGRI (extrapolated to 2–200 keV).

[b]Fits of this interval also include simultaneous *RXTE* data. Note that if the normalization constant is frozen to 1.0 for PCA, the one we obtain
from the fit for ISGRI is 0.952 and that for JEM-X 1.016.

FIG. 1.— Zoom on one cycle from each of the three observations with cycles. From top to bottom, the panels respectively represent the Ryle 15GHz, the JEM-X 3–13 keV, the ISGRI 18–50 keV lightcurves and the 3–13 keV/18–50 keV HR. The different intervals from which spectra were extracted are indicated with letter on the JEM-X light curve.
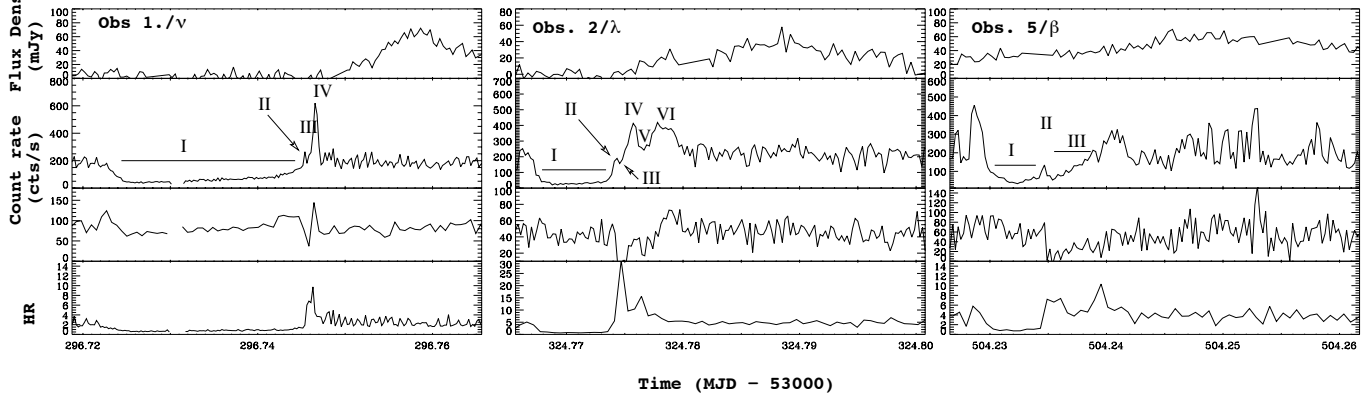

FIG. 2.— Joint JEM-X and ISGRI spectra from the four intervals of Obs. 1/class ν. The best-fit model is superposed onto the spectra, as well as the individual components, a disk and a Comptonized tail. The best fit parameters are given in Table 1.
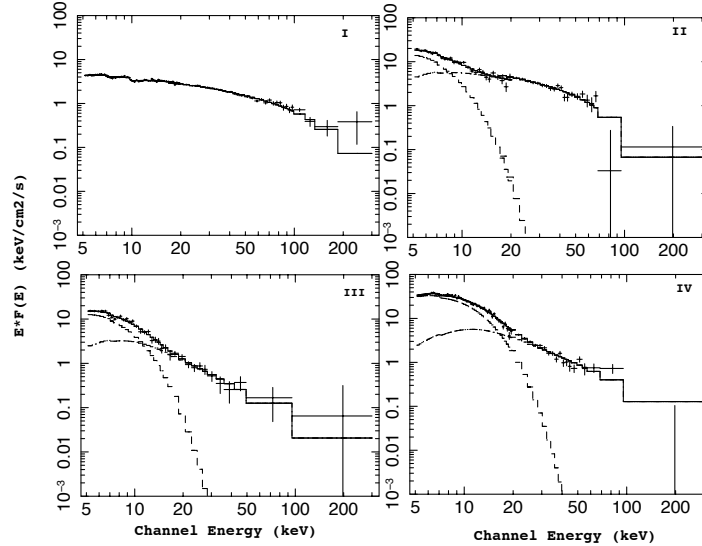
FIG. 3.— Dynamical power spectrum (top) and PCA light curve (bottom) from the three observations with cycles. a) ν-type cycle simultaneously observed with *RXTE* and *INTEGRAL*. b) λ-type cycles observed with *RXTE*. c) β-type cycle observed with *RXTE*. The gray scale represents the RMS power of the variability, with white having a higher power than dark points.
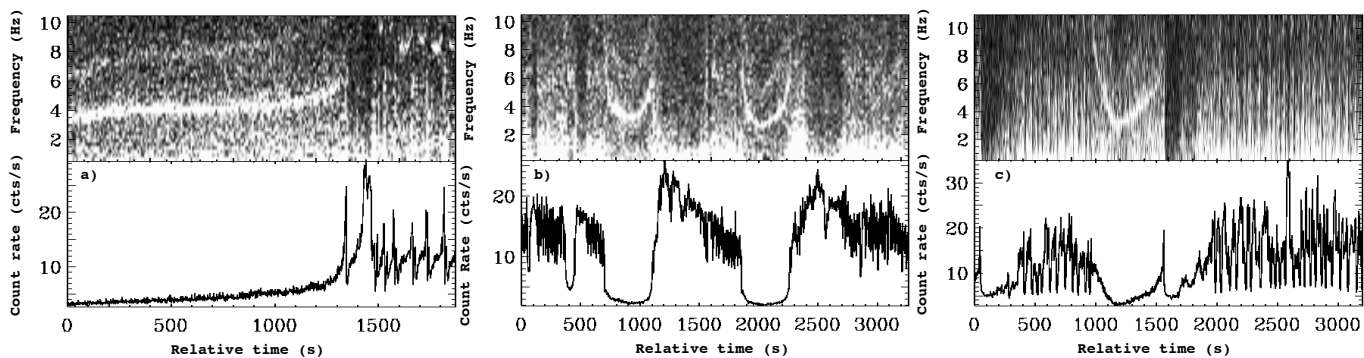
Fig. 4.— Zoom on the interval of Obs. 4. from which we extracted the time dependent spectra. From top to bottom, the panels respectively represent the Ryle 15GHz, the JEM-X 3–13 keV, the ISGRI 18–50 keV, and PCA 2–60 keV lightcurves. The different intervals from which spectra were extracted are indicated with the letter on the light curves. The best fit parameters are given in Table 2.
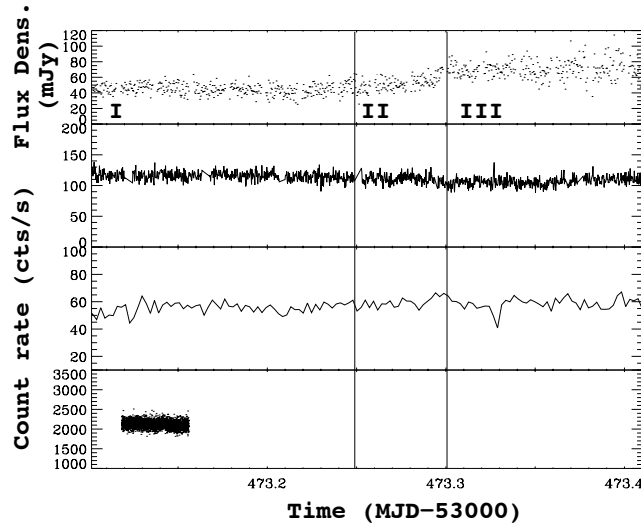

Fig. 5.— **Left:** Residuals in terms of σ between the models used to fit the *RXTE* spectra. In each case the model mentioned in the panel is convolved with interstellar absorption. Pl stands for power law and ga stands for Gaussian. From top to bottom the reduced χ^2 are the following: 25.2 (132 d.o.f.), 7.3 (131 d.o.f.), 5.5 (129 d.o.f.) and 1.8 (126 d.o.f.). **Right:** Joint *INTEGRAL+RXTE* spectra from Obs. 4 Int. I. The best model (consisting of a `comptt` a power law and a Gaussian convolved by absorption) is superposed on the spectra.
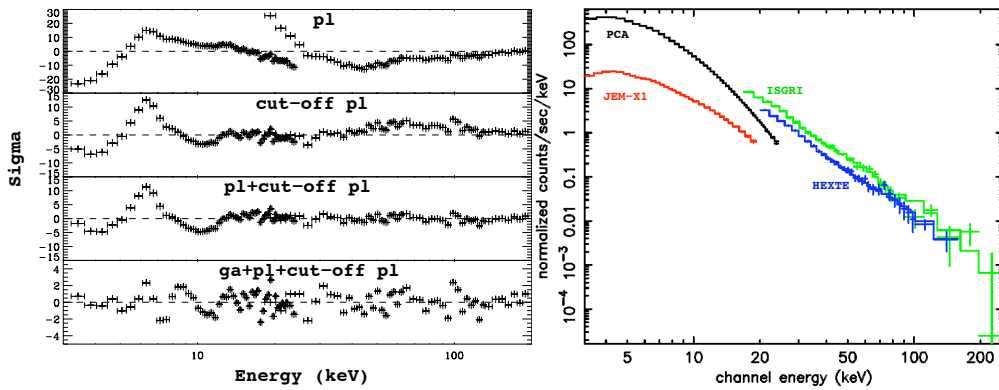

Fig. 6.— Spectrum of the LFQPO from the unique *RXTE* observation that was simultaneous to *INTEGRAL* Obs. 4 and the RT. The best model obtained from fits with power law and power law with an exponential cut-off are respectively over-plotted as a dash-dotted and a dashed line. A better fit is obtained with the power law with cut-off.
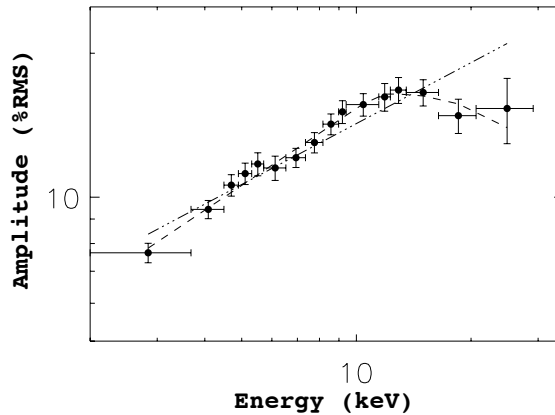
FIG. 7.— Hardness-Intensity diagrams of the four observations discussed in the paper. Each point represents 16s. **Left:** PCU 2 count rate vs. (6.1–10.2) keV/(3.3–6.1) keV. **Right:** PCU 2 count rate vs. (14.8–40.4) keV/(3.3–6.1) keV. The dashed line is roughly indicative of the position of the jet line: each time GRS 1915+105 transits from the dip through this line an ejection occurs.
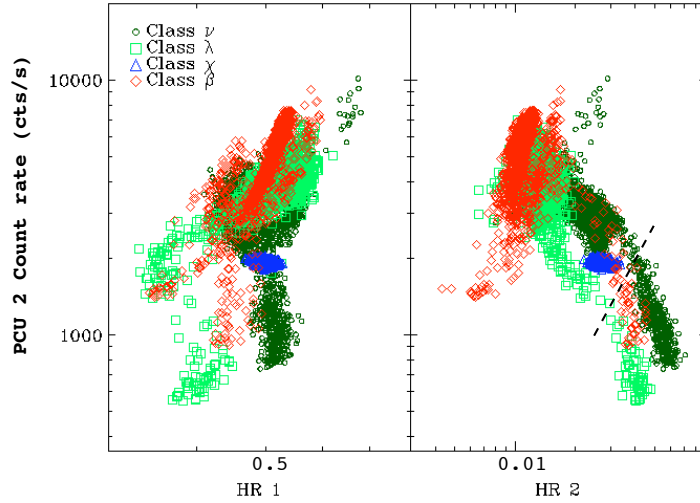

FIG. 8.— **Top panel:** *RXTE*/PCA spectrum of Obs. 4 Int. A (bullet). The best fit model, the power law component, and the `comptt` component are over plotted. **Bottom panel:** Relative contribution of the `comptt` component and spectrum of the QPO.